*Dedicated to Professor Dr. rer. nat. Wolfgang Pitsch on the occasion of his 65th birthday*

# High-speed temperature measurements during rapid solidification of iron-silicon ribbons, produced by planar flow casting

**Georg Frommeyer and Andreas Ludwig**

In order to investigate the melt undercooling and the non-equilibrium solidification of crystalline Fe 5 wt.% Si melt spun ribbons, produced by planar flow casting (PFC), high speed temperature measurements and appropriate process simulations have been performed. Using a rotating fibre optical system with a fast response double pyrometer, the temperature radiation of the solidifying ribbon during the casting process has been recorded with a measuring frequency of 50 kHz. The obtained cooling curves have been interpreted by computer simulations. It is shown that with increasing wheel temperature the overall cooling becomes more efficient. This is caused by an improved wetting behaviour of the melt-wheel system and an increase in the heat transfer coefficient at the interface of the solidifying ribbon and the wheel from $6 \cdot 10^4$ to about $2 \cdot 10^5$ W/(m$^2$K). The solidification of 100 to 200 $\mu$m thick ribbons takes place in a time interval of 2 to 5 ms. The average growth rate varies between 10 and 60 mm/s. The high cooling rate results in a fine dendritic solidification morphology with diminishing microsegregations.

**Hochgeschwindigkeits-Temperaturmessungen während der raschen Erstarrung beim Dünnbandgießen von Eisen-Silicium nach dem Planar Flow Casting.** Zur Untersuchung der Schmelzenunterkühlung in der Band-Rad-Kontaktzone und der Nichtgleichgewichtserstarrung mikrokristalliner Fe-5Gew.%-Si-Meltspinbänder während des Planar Flow Casting (PFC)-Verfahrens wurden Hochgeschwindigkeits-Temperaturmessungen mit begleitenden Prozeßsimulationen durchgeführt. Die Temperaturstrahlung der Schmelze und des erstarrenden Bandes wurde mit einer Glasfaseroptik unter Verwendung eines schnell ansprechenden Quotientenpyrometers mit einer Meßfrequenz von 50 kHz aufgezeichnet. Die gemessenen Abkühlkurven wurden mit numerischer Prozeßsimulation interpretiert. Die Ergebnisse zeigen, daß die Abkühlung mit steigender Radoberflächentemperatur effizienter wird. Dieses ist durch die verbesserte Benetzungsfähigkeit der Schmelze und zunehmende Wärmeübergangskoeffizienten zwischen dem erstarrenden Band und der Radoberfläche von $6 \cdot 10^4$ auf $2 \cdot 10^5$ W/(m$^2$K) bedingt. Die Erstarrung von Meltspinbändern mit Dickenabmessungen von 100–200 $\mu$m ist im Zeitintervall von 2 bis 5 ms abgeschlossen. Daraus ergeben sich Kristallwachstumsraten von 10–60 mm/s. Die hohe Abkühlrate verursacht eine feinstrukturierte dendritische Erstarrungsmorphologie mit verringerter Mikrosegregation.

The development of metastable microstructures by *r*apid *s*olidification *p*rocessing (RSP) has received wide attention in recent years[1)2)]. The most important aspects of this topic are the relations between the heat flow characteristics, the solidification rates, and the resultant microstructures. The high undercooling at the wheel contact zone results in a transient solidification where the formed nuclei grow into undercooled melt areas. This leads to metastable and featureless microstructures in the chill zones of the ribbons. On-line temperature measurements during rapid solidification are the keypoint for a better understanding of the influence of RSP parameters on the formation of the microstructure.

In the last decade several techniques have been applied to determine the temperature distribution in rapidly solidifying melt spun ribbons during their continuous production by *p*lanar *f*low *c*asting (PFC). Davies et al. and Cantor et al. employed photocolorimetry[3)–6)]. Mühlenbach et al. performed thermovision[7)8)], and Vogt et al. applied fast response infrared pyrometry[9)10)]. For photocolorimetric or thermovision measurements the temperature dependence of the emissivity of the as-cast alloy has to be known. Due to the limited number of data points the quantitative temperature determinations by a set of infrared pyrometers provide insufficient information about the temperature distribution in the liquid-solid phase transition region.

The present paper describes a new fibre optical system to detect the temperature radiation of rapidly solidifying melt spun ribbons with a measuring frequency of 50 kHz, based on high speed double pyrometry. In order to analyze the experimentally determined cooling curves a numerical model has been evaluated. This takes the melt undercooling at the wheel contact zone, the corresponding temperature gradient in the solid and the liquid, and the resulting growth rate into account. The KGT-theory, named after W. *K*urz, B. *G*iovanola, and R. *T*rivedi[11)], was used to model the constrained dendritic growth of rapidly solidified iron silicon foils. The simulation reveals that the solidification is related to the shape of the measured cooling curves. In addition a decrease in the heat transfer coefficient $h$ is predicted. This is consistent with the results of SEM-investigations. The average growth rate for the solidification of Fe 5 wt% Si melt spun ribbons, 100–200 $\mu$m in thickness, has been determined and the effect of the growth rate on the morphology and the appearing microsegregation will be considered.

## Experimental procedure

In order to detect the temperature radiation of the melt and of the solidifying ribbon the melt spinning facility at the MPI für Eisenforschung[9)] was equipped with a rotating mirror-lens-system, adjusted to the wheel. The fibre optic diverts the radiation to a coupling on the wheel axes. **Figure 1a** illustrates the measuring device, and the schematic drawing of **figure 1b** shows the mirror-lens-system which is focussed on the middle zone of the melt stream and the solidifying ribbon.

From the coupling on the wheel axes the radiation is guided into a second optical fibre. This diverts the signal into a double pyrometer, where the radiation is divided into

*Professor Dr.-Ing. Georg Frommeyer*, Department of Materials Technology, Max-Planck-Institut für Eisenforschung GmbH, Düsseldorf; Dr.rer.nat. *Andreas Ludwig*, Foundry Institute, RWTH Aachen, Germany.

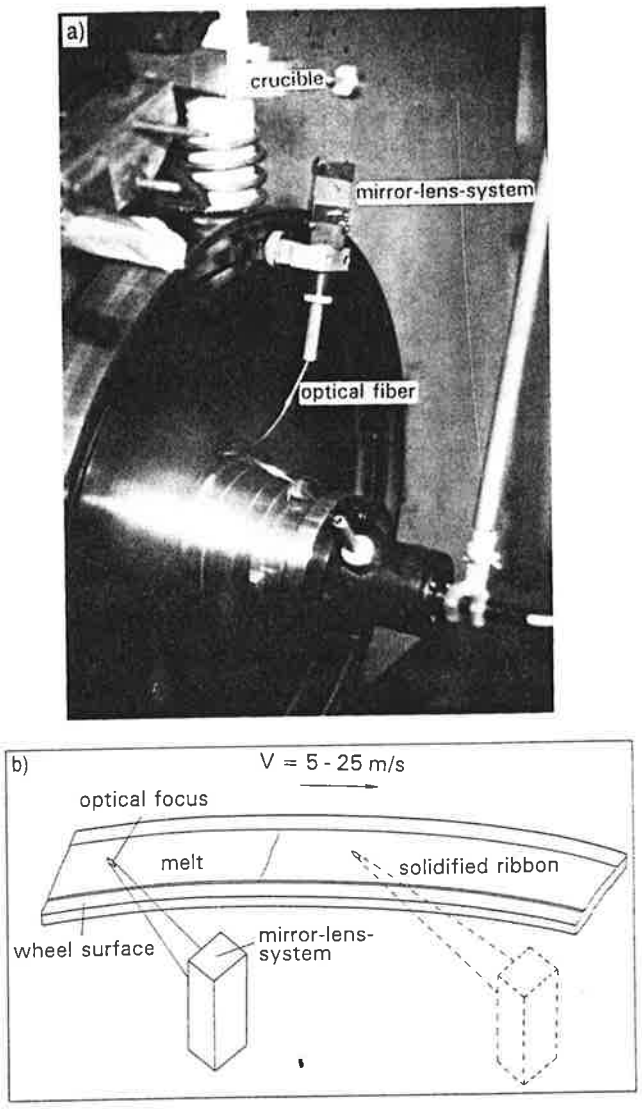


**Figure 1.** Fibre optical device for measuring the temperature radiation during the formation of ribbons by the PFC-process (a). Schematic drawing of the focussing mirror-lens-system for measuring the temperature radiation of the rapidly solidifying melt and ribbon (b)

two optically equivalent rays with slightly different wave lengths. These are registered by photodiodes. The wavelength selection was performed by two interference filters with the characteristic wave lengths: $\lambda_1 = 920$ nm and $\lambda_2 = 1040$ nm and a band width of $\pm$ 40 nm. Using a 100 $\Omega$ resistance the intensity of the temperature radiation, which is proportional to the photovoltage, is trapped and amplified by a low noise operational amplifier. The obtained data were stored simultaneously using a transient recorder (type: TC-ADAM 1024, 2 MHz, 10 bit). **Figure 2** represents the block diagram of the double pyrometer with the amplifiers and the transient recorder.

The detected voltage $U$ of a photodiode is related to the radiation temperature $T$ by Wien's law:

$$U(\lambda, T) = A_\lambda \cdot J(\lambda, T) = A_\lambda \cdot \varepsilon(\lambda, T) \cdot \frac{8\pi hc^2}{\lambda^5} \cdot e^{-\frac{hc}{\lambda k_B T}}, \quad (1)$$

$A_\lambda$ is a wavelength dependent factor, which takes the amplification of the voltage as well as the absorption of the radiation by the optical components into account; $J$ defines the energy density of the heat radiation; $\varepsilon$ is the temperature dependent emissivity at a given wavelength $\lambda$; $h$ is the Planck's and $k_B$ is the Boltzmann's constant; $c$ is the speed of light.

The photovoltage ratio of two different wavelengths $\lambda_1$ and $\lambda_2$ is described by the following equation:

$$\frac{U_1(\lambda_1, T)}{U_2(\lambda_2, T)} = a \left(\frac{\lambda_1}{\lambda_2}\right)^{-5} \exp\left(-\frac{hc}{k_B T}\left(\frac{1}{\lambda_1} - \frac{1}{\lambda_2}\right)\right) \quad (2)$$

where

$$a \equiv \frac{A_{\lambda_1}}{A_{\lambda_2}} \frac{\varepsilon(\lambda_1, T)}{\varepsilon(\lambda_2, T)}.$$

For the two sligthly different wavelengths $\lambda_1$ and $\lambda_2$, the temperature dependence of the emissivities is nearly equal and the factor $a$ is independent of the temperature. Thus measuring the voltage ratio $U_1/U_2$ at a given temperature $T$ the factor $a$ can be estimated. An appropriate calibration has been performed by annealing Fe 5 wt.% Si melt spun ribbons in a protecting argon atmosphere. This enables an equivalent comparison of the measured thermovoltages with the detected diode voltage of the fibre optical system. The experimentally determined factor $a$ exhibits an inaccuracy of about $\pm$ 3 %.

During continuous casting the rotating mirror-lens-system reflects the temperature radiation from a 2 mm$^2$ spot size of the middle part of the solidifying ribbon into the optical system. When the photovoltages of the two diodes exceed the trigger level of 4 V, the detector signals are stored. The reading is completed in 20 ms. After one wheel rotation the second measurement of the temperature radiation is carried out automatically. This enables the on-line recording of subsequent photovoltage vs. time curves in constant time intervals of the PFC-process. The related cooling curves $T$ vs. $\tau$ were calculated by equation (2).

The response time of the photodiodes and of the transient recorder is less than 500 ns and that of the operational amplifiers is of the order of 20 $\mu$s. Using a fast luminescence diode a maximum measuring frequency of 50 kHz for the electronic system is achieved.

For the investigation of the melt undercooling at the wheel contact zone and the non-equilibrium solidification high speed temperature measurements have been carried out during the continuous casting of Fe 5 wt.% Si melt spun ribbons on a mild steel wheel. The velocity was about

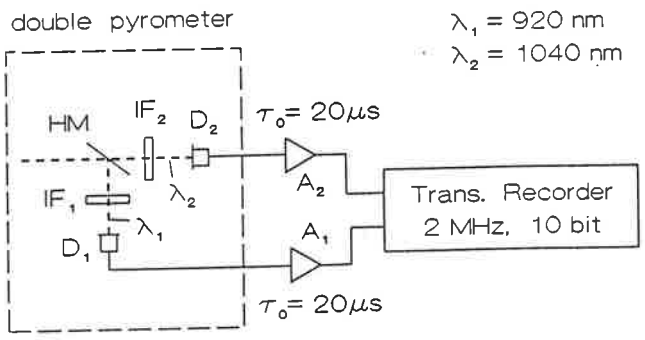


**Figure 2.** Block diagram of the applied double pyrometer with amplifier and transient recorder (HM – semi-transparent mirror, IF – interference filter, D – photodiode, A – amplifier)

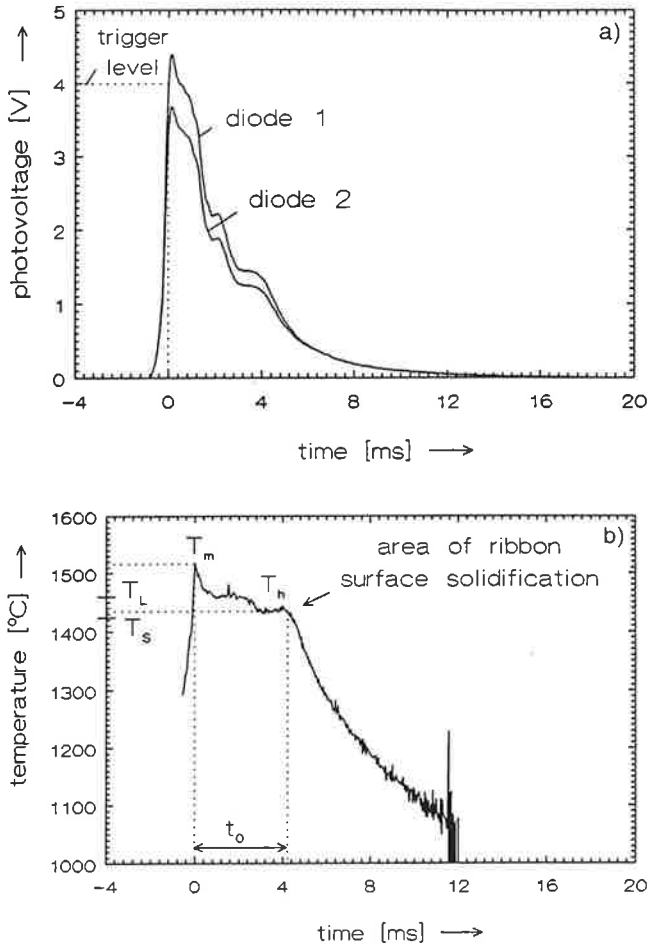


**Figure 3.** Characteristic photovoltage vs. time curve obtained by the fibre optical measuring system (a), and the related temperature vs. time cooling curve (b) of a rapidly solidified melt spun ribbon

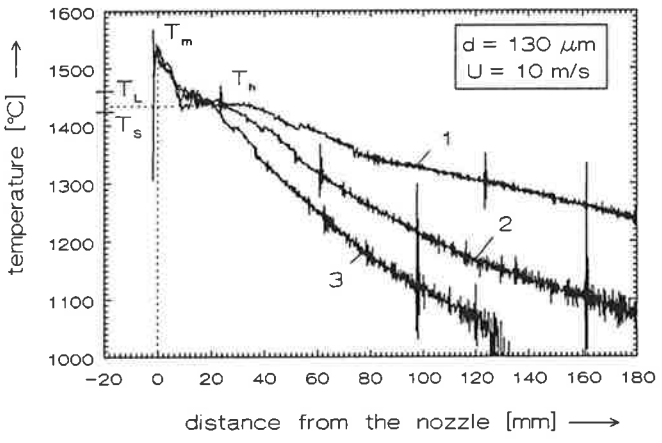


**Figure 4.** Cooling curves of three successive solidification procedures during the continuous PFC-process marked by the chronological order of the wheel rotation ($T_m$ – maximum, $T_h$ – plateau, $T_l$ – liquidus, $T_S$ – solidus temperature)

10 m/s. The melt spinning facility and technical details of the PFC-process are described elsewhere[9]).

The measured cooling curves were simulated using a numerical model which is based on the two-dimensional thermal transport equation. The heat release during the solidification is taken into account by a source term similar to the 'effective specific heat capacity method'. For the explicit finite difference calculation the melt puddle geometry is fitted on a rectangular grid. The heat transport through the melt-wheel interface is described by the heat transfer coefficient $h_1$, whereas the heat transfer between the solidifying ribbon and the roller is defined by $h_2$. The heat radiation of the free melt or ribbon surfaces is neglected.

It is stated that a heterogeneous nucleation at the melt-wheel interface initiates the solidification. Because of the unknown governing parameters of the heterogeneous nucleation and especially the transient effects, which might be important at high cooling rates[12]), undercooling necessary for the nucleation is treated as an external parameter. The growth rate during the solidification process has been estimated by the KGT-theory for constrained dendritic growth with high Péclet-numbers[11]). The micro-segregation has b een described by the model of Giovanola and Kurz[13]). For further details of the numerical model the reader is referred to[14])-[17]).

## Results

**Figure 3a** exhibits a recorded photovoltage vs. time plot, and the related temperature vs. time cooling curve is shown in **figure 3b**. Three successive cooling curves of an iron silicon ribbon, 130 $\mu$m in thickness and 30 mm in width, continuously cast with a wheel velocity of 10 m/s are represented in **figure 4**. The curves are marked in their chronological order. Starting with $T_m \simeq 1520$ °C, the temperature decreases to a plateau at $T_h \simeq 1440$ °C, which lies in the liquidus ($T_l = 1465$ °C) and solidus ($T_s = 1425$ °C) interval on the iron rich side of the iron-silicon phase diagram. $T_m$ is related to the rear edge of the nozzle, where the melt leaves the nozzle-wheel-gap. After remaining at $T_h$ for a period of about 2–3 ms, which corresponds to a distance of 20–30 mm from the rear edge of the nozzle, the temperature decreases continuously. In the high temperature regime no significant differences in the cooling curves occur. Whereas below the temperature plateau, the curves reveal considerable dissimilarities. The overall cooling rate increases from $\dot{T} \simeq 1.5 \cdot 10^4$ K/s for the first cooling curve to $\dot{T} \simeq 3.7 \cdot 10^4$ K/s for the third one. The temperature of the preheated wheel increases from 200 °C at the beginning of the casting process to about 450 °C after three wheel revolutions.

Because of the limited amount of the melt (about 300 g) in the crucible the PFC-process time is about 1 s, which results in six or seven wheel revolutions. This allows six repeated cooling runs to be measured. All studied casting processes experienced an improvement in the cooling behaviour as demonstrated by the steeper slopes of the cooling curves[17]). Thus for the performed casting experiments no steady state is achieved during the process time. Due to the strong influence of the wheel surface temperature and the surface oxidation on the cooling rate and the heat transfer, the cooling curves obtained for the same process parameters were not identical. Even thin ribbons experience lower cooling rates than thicker ones if the wetting of an oxidized wheel surface is deteriorated.

Typical recalescence phenomena were not observed on the surface of the melt pool and the solidifying ribbon. Average cooling rates, calculated from the measured cooling curves for the temperature interval from $T_m$ to 1100 °C, are of the order of $6 \cdot 10^4$ K/s.

Numerical process simulations, taking the influence of the melt undercooling and heat transfer coefficients on the surface temperature of the melt pool and the solidifying ribbon into account, reveal that the solidification is related to the shape of the measured cooling curves. **Figure 5a** shows a calculated cooling curve where the marked edge correlates with the solidification stages of the formed ribbon. Analogous to the results of the on-line temperature measurements, the calculated melt puddle surface temperature decreases steadily to a constant plateau temperature. **Figure 5b** represents a cross-sectional view of the melt pool with the plotted mushy zone. The solidification is caused by surface induced heterogeneous nucleations on a planar liquid-solid interface. Due to the latent heat release the interface temperature increases, leading to a decreasing growth rate of 200 mm/s in the chill zone. This causes the change from planar to dendritic growth morphology. The initial growth velocity is larger than the solute limit of absolute stability ($V^c_{abs} \approx 280$ mm/s) leading to a planar growth morphology at the beginning of solidification. The solute limit of absolute stability is quantitatively described by the following equation:

$$V^c_{abs} = \frac{\Delta T_0 \cdot D_i}{k \cdot \Gamma}. \qquad (3)$$

$\Delta T_0$ is the liquidus-solidus temperature interval at a given concentration $C^i_0$; $D_i$ defines the partial diffusion coefficient

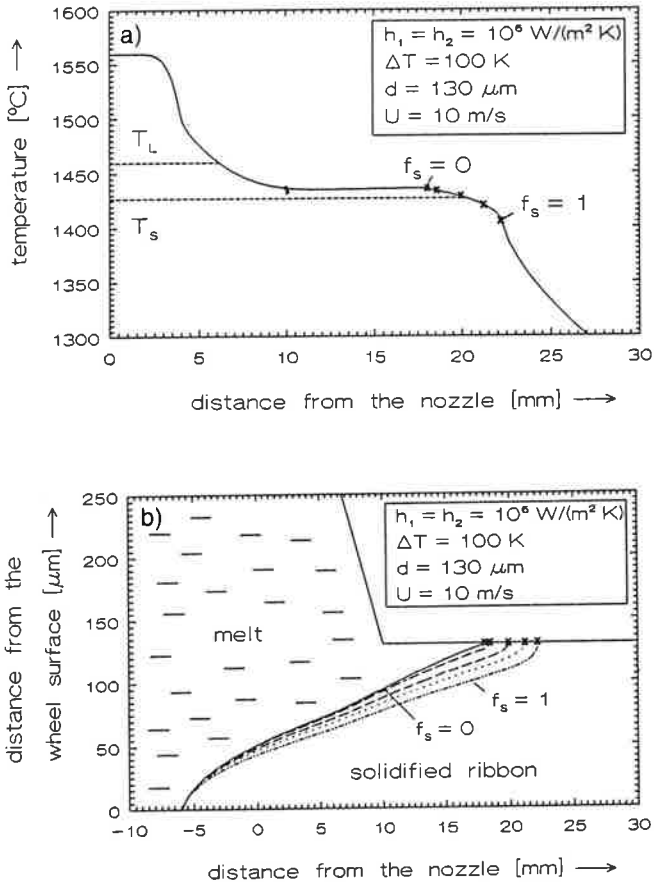


**Figure 5.** Calculated cooling curve with the marked area of the solidifying ribbon surface for the given process parameters (a). Cross-section of the melt pool where the ribbon is formed with plotted mushy zone. $f_s$ describes the volume fraction of the solidified melt (b)

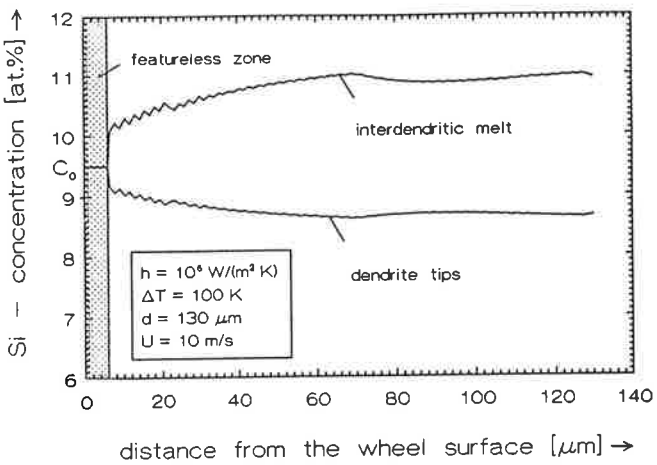


**Figure 6.** Silicon concentration of the solidified cells or primary dendrites and of the interdendritic melt as a function of the distance from the wheel surface for an Fe 5wt.% Si (9.5 at.% Si) melt spun ribbon ($d$ = 130 $\mu$m)

of the component $i$ in the melt; $k$ is the distribution and $\Gamma$ expresses the Gibbs-Thompson coefficient.

The corresponding mushy zone is indicated by the dotted area, and $f_S$ describes the relative amount of solid. $f_S = 1$ represents the dendrite roots and $f_S = 0$ the dendrite tips.

The solidification of the interdendritic melt is complete when the actual temperature is below the solidus line. From the extension of the temperature plateau of the experimentally determined cooling curves and the ribbon thickness of 130 $\mu$m the solidification time interval and the average growth rate were estimated. The cast melt spun ribbon solidifies within 3 ms with an average solidification rate of about 40 mm/s.

The silicon concentration of the dendrites and the interdendritic melt is derived from the solidification rate of the growing dendrites as a function of the distance from the wheel surface, taking the GK-model into account. **Figure 6** represents the silicon concentration curves of the primary dendrites (lower curve) and of the interdendritic melt (upper curve) in dependence on the distance from the wheel surface. The thickness of the chill zone, illustrated by the dotted region, is about 6 or 8 $\mu$m. In the chill zone the solidification rate is oscillating and the silicon content varies around the nominal concentration of $C_0 = 9.5$ at%. The distinct concentration curves of the primary dendrites and the interdendritic melt are divergent with increasing distance from the chill zone up to 70 $\mu$m and then proceed constantly up to the total ribbon thickness of 130 $\mu$m. The final silicon concentration difference is about 2.5 at.%. The microstructure of the longitudinal section is shown in **figure 7**. The chill zone exhibits an extremely fine-grained structure whereas the columnar dendritic crystals consist of primary dendritic cells with low angle grain boundaries.

The temperature distribution at the dendrite tips and the solidification temperature of the interdendritic melt is plotted in **figure 8**. The chill zone reveals a temperature oscillation whereas the dendrite tip temperature lies in between the solidus and liquidus lines of the iron silicon alloy. The interdendritic melt temperature is about 20 °C below the solidification temperature. This undercooling is caused by a silicon enrichment in the interdendritic melt.

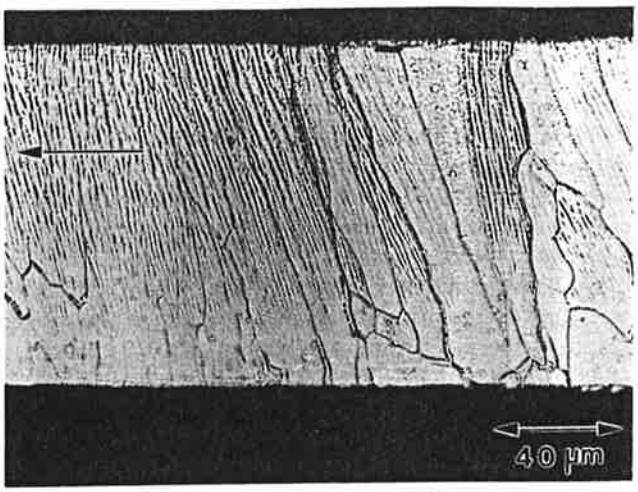


**Figure 7.** Microstructure of a rapidly solidified Fe 5wt.% Si ribbon, $d$ = 130 $\mu$m thick and 30 mm in width, in longitudinal section. The chill zone of the ribbon-wheel contact side reveals an equiaxed grain structure whereas the columnar grains consist of primary dendrites

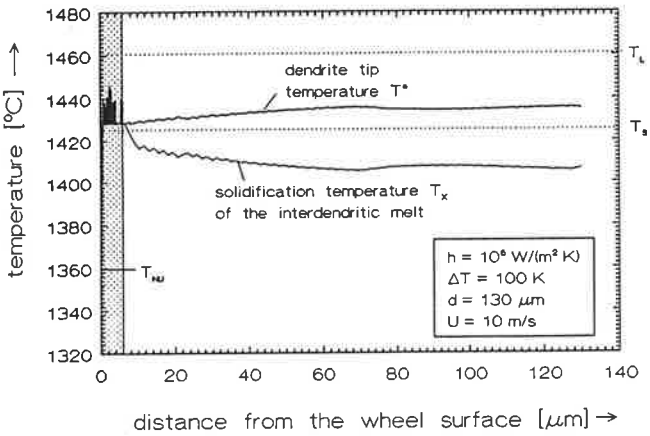


**Figure 8.** Temperature distribution at the planar liquid/solid interface (chill zone), at the tips of the solidified cells or primary dendrites $T^*$, and the solidification temperature of the interdendritic melt $T_x$ in dependence on the distance of the wheel surface

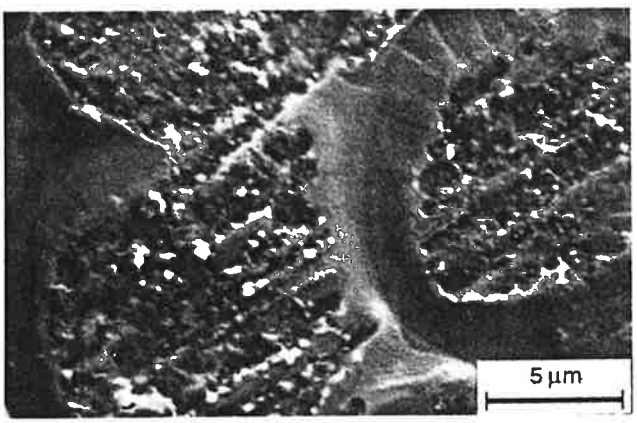


**Figure 9.** SEM-micrograph showing the contact surface of an iron silicon melt spun ribbon. The smoothly solidified grain boundaries occur due to local shrinkage of the rest melt between the solidifying grains. The contact grain surfaces revealing the marks of the wheel topology

## Discussion

For the evaluation of the heat transfer coefficient the measured and the calculated cooling curves were compared. Extensive parameter studies revealed that the measured cooling curves cannot be fitted in the whole temperature range from $T_m$ to 1100 °C by using one constant heat transfer coefficient. The calculated curves reveal a faster cooling rate than the experimentally determined one. The discrepancy is explained by a decrease in the heat transfer between the solidifying ribbon and the wheel. The high heat transfer coefficient $h_1 = 2 \cdot 10^5$ W/m$^2$K is changed to a lower value of $h_2 = 6 \cdot 10^4$ W/m$^2$K, when the distance from the dendrite tips to the wheel surface exceeds $d_x$ = 50 $\mu$m.

In order to interpret the decrease in the heat transfer during rapid solidification of a thin layer on a metallic substrate SEM-investigations of the ribbon contact surface have been performed. In addition to the observed air pockets[18][19], the contact surface of the ribbon exhibits a fine network of smooth non-planar areas on grain boundaries, whereas the central regions of the grains were in close contact with the wheel surface, revealing typical marks of the wheel surface topology, **figure 9**.

Due to the large heat transfer coefficient of the melt-wheel interface of about $h_1 = 5 \cdot 10^6$ W/(m$^2$K) ideal cooling conditions occur. When nuclei are formed by surface-induced heterogeneous nucleation, the solidification and growth of separate grains takes place by an intense contact with the wheel surface. The volume shrinkage of the solidifying grains causes a local lifting up of the melt zone between the growing crystals. This results in the smooth topology of the grain boundaries. Consequently, the effective contact area is decreasing, and the overall heat transfer coefficient which is interpreted as a macroscopic quantity averaging over a certain contact area is lowered. This continuous change in $h$ was taken into account as a discontinuous one by the first order approximation in the process simulation.

Rapid substrate quenching on a rotating wheel with an elevated surface temperature of about 200 °C results in a considerable change in $h$ during the solidification from $h_1 = 5 \cdot 10^6$ W/(m$^2$K) – melt-wheel contact – to about $h_2 = 6 \cdot 10^4$ W/(m$^2$K) – solidified ribbon-wheel system – of two orders of magnitude, respectively, **figure 10**. During the PFC-process the mild steel wheel surface temperature increases of 30–50 °C per wheel rotation. In the total process time the maximum surface temperature is about 600 °C. In this case the heat transfer coefficient decreases from $h_1 = 5 \cdot 10^6$ W/(m$^2$K) to a somewhat lower value of $h_2 = 2 \cdot 10^5$ W/(m$^2$K). The wheel temperature strongly influences the heat transfer between the solidifying ribbon and the wheel surface.

This is in agreement with the results reported by R.E. Maringer[20]. It was shown that in drop-splat experiments a critical sticking temperature $T_c$ exists, where the melt droplets stick on an inclined metallic substrate surface after solidification. $T_c$ is characteristic for a selected melt-substrate combination. If the substrate temperature is higher than $T_c$ internal stresses in the solidified splats, induced by thermal contraction, will be released either in the droplets or in the substrate. In addition to this interpretation it has to be considered that an oxide layer on the wheel surface is piled up during the casting process. By each wheel ro-

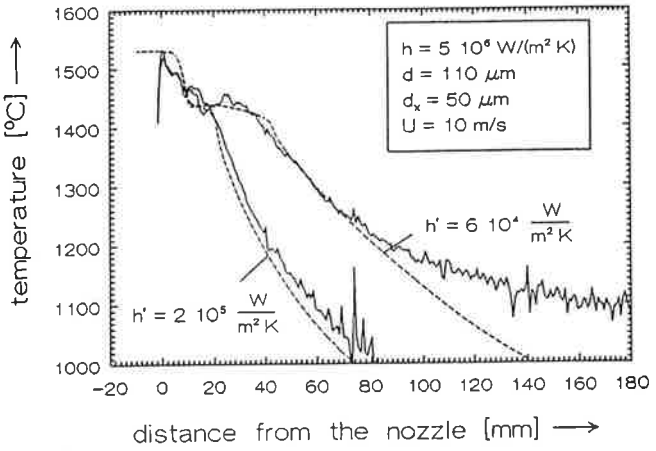


**Figure 10.** Comparison of the measured and the calculated cooling curves. In order to fit the experimentally determined cooling curve, $h_1$ is reduced to $h_2$ after primary solidification of a layer of $d_x$ = 50 µm from the wheel-ribbon contact zone

tation the up-lifting ribbons partly remove the oxide layer which is formed during the preheating of the wheel. For a quantitative analysis of the heat transfer mechanisms further investigations will be carried out in greater detail.

Because of the efficient heat extraction by the substrate the melt is undercooled within the incubation time of the transient nucleation. A comparison of the microstructures of highly undercooled alloys with those of rapidly quenched copper nickel ribbons reveals that the degree of undercooling is extremely high and exceeds more than 200 K[21]). By numerical process simulations, the undercooling at the wheel contact zone has been varied by changing the starting time of solidification. The results showed that due to the high heat transfer coefficient of $h_1 = 5 \cdot 10^6$ W/(m$^2$K) under the melt pool, the undercooling of 200 K occurs in a thin melt layer of about 6 or 8 µm in thickness. The thin undercooled layer in contact with the wheel is heated up by the latent heat release in the first solidification stage, resulting in a directional growth situation. The crystals grow almost perpendicular to the wheel surface in radial direction parallel to the positive temperature gradient of $10^7$ K/m in the solid and the liquid. The tangential temperature gradient is relatively low and can be neglected. The extremely high solidification rate and the steep temperature gradient cause growth rates of the primary dendrites of about 25 mm/s. The temperature of the melt puddle surface is not lower than the actual interface temperature and does not decrease before the solidification is completed.

According to this, the lower edge of the temperature plateau is related to the solidification which takes place on the ribbon surface, and the decrease in the temperature under the plateau is related to the cooling stage of the solidifying ribbon within 2 to 5 ms.

The performed correlation of the calculated actual solidification time of 3 ms for the ribbon thickness of 130 µm results in an average growth rate of about 40 mm/s. Compared with the upper limit of absolute stability for directional growth, which is 280 mm/s for the Fe 5 wt.% Si alloy, the estimated growth rate is fairly high and causes a fine-structured growth morphology of the rapidly solidified iron silicon cells or primary dendrites with diminishing microsegregations[19]). These facts correspond well with the observed cellular substructure in the columnar grains of cross-section of the ribbon and the microcrystalline dendrites on the ribbon surface[22])[23]). Compared with conventional casting processes, where growth rates of the order of 1 µm/s are common, the high solidification rate during the PFC-process leads to a suppression of the B2 and $DO_3$ ordering phases in FeSi melt spun ribbon[24]).

## Acknowledgement

The authors gratefully acknowledge the financial support from the Deutsche Forschungsgemeinschaft under the Contract No. Fr. 543/7.

(A 00714; received: 11. May 1992)

## References

[1]) *Duwez, P.; Willens, R.W.; Klement, W.:* J. Appl. Phys. 36 (1960), p. 1136/44.
[2]) *Jones, H.:* Rapid Solidification of Metals and Alloys, Institution of Metallurgists, London. 1982.
[3]) *Tenwick, M.J.; Davies, H.A.:* Proc. 5th Int. Conf. on Rapidly Quenched Metals, [eds.:] S. Steeb, H. Warlimont, Elsevier (1985) p. 67/70.
[4]) *Vincent, J.H.; Hebertson, J.G.; Davies, H.A.:* Proc. 4th Int. Conf. on Rapidly Quenched Metals, Sandai (1981), p. 77/81.
[5]) *Gillen, A.G.; Cantor, B.:* Acta Metall. 33 (1985), p. 1813/25.
[6]) *Bewlay, B.P.; Cantor, B.:* Int. J. of Rapid Sol. 2 (1986), p. 107/23.
[7]) *Mühlenbach, H.; Stephani, G.; Sellger, R.; Fiedler, H.:* Int. J. Rapid Sol. 3 (1987), p. 83/94.
[8]) *Stephani, G.; Mühlenbach, H.; Fiedler, H.; Richter, G.:* Mat. Sci. Eng. 98 (1988), p. 29/32.
[9]) *Vogt, E.; Frommyer, G.:* Proc. 1st Int. Conf. on Rapidly Solidified Material, San Diego (1986), p. 291/97.
[10]) *Vogt, E.:* Int. J. Rapid Sol. 3 (1987), p. 131/46.
[11]) *Kurz, W.; Giovanola, B.; Trivedi, R.:* Acta Metall. 34 (1986), p. 823/30.
[12]) *Kelton, K.F.; Greer, A.L.:* J. Non-Cryst. Solids 79 (1986), p. 295/309.
[13]) *Giovanola, B.; Kurz, W.:* Metal. Trans. 21A (1990), p. 260/63.
[14]) *Gránásy, L.; Ludwig, A.:* Proc. of the Int. Conf. on Solidification and Microgravity, Miskoloy, Hungary (1991).
[15]) *Gránásy, L.; Ludwig, A.:* Proc. of the Symposium 'Melt-Spinning and Strip Casting' of the TMS Annual Meeting, San Diego (1992), in print.
[16]) *Ludwig, A.; Gránásy, L.; Frommeyer, G.:* to be published.
[17]) *Ludwig, A.:* Flüssig-Fest-Phasentransformation von FeSi 5 Gew.%-Legierungen unter Nichtgleichgewichtsbedingungen, Dr.-rer.nat.-Diss., RWTH Aachen, 1992.
[18]) *Huang, S.C.; Fiedler, H.C.:* Met. Trans. 12A (1981), p. 1107/12.
[19]) *Ludwig, A.; Frommeyer, G.:* Proc. of the Symposium 'Melt-Spinning and Strip Casting' of the TMS Annual Meeting, San Diego (1992), in print.
[20]) *Maringer, R.E.:* Mater. Sci. Eng. 98 (1988), p. 13/20.
[21]) *Caesar, C.; Köster, U.; Willnecker, R.; Herlach, D.M.:* Mat. Sci. Eng. 98 (1988), p. 339/42.
[22]) *Kurz, W.; Fischer, D.J.:* Fundamentals of Solidification, Trans. Tech. Publications, Aedermannsdorf (1989).
[23]) *Vogt, E.; Frommeyer, G.:* Z. Metallkde. 78 (1987), p. 263/67.
[24]) *Wittig, J.E.; Vogt, E.; Frommeyer, G.:* Ultramicroscopy 30 (1989), p. 172/80.